nanomaterials

MDPI

Article

Boosting the Oxygen Evolution Reaction by Controllably Constructing $FeNi_3$/C Nanorods

Xu Yu [1,*], Zhiqiang Pan [1], Zhixin Zhao [1], Yuke Zhou [1], Chengang Pei [1], Yifei Ma [2], Ho Seok Park [3] and Mei Wang [2,*]

[1] School of Chemistry and Chemical Engineering, Yangzhou University, Yangzhou 225009, China; w461015600@163.com (Z.P.); zhao1zhi2xin3@163.com (Z.Z.); zykds66@163.com (Y.Z.); chengpyzu@163.com (C.P.)

[2] State Key Laboratory of Quantum Optics and Quantum Optics Devices, Institute of Laser Spectroscopy, Collaborative Innovation Center of Extreme Optics, Shanxi University, Taiyuan 030006, China; mayifei@sxu.edu.cn

[3] Department of Chemical Engineering, College of Engineering, Sungkyunkwan University, 2066 Seobu-ro, Jangan-gu, Suwon-si 440-746, Gyeonggi-do, Korea; phs0727@skku.edu

* Correspondence: yxypz15@yzu.edu.cn (X.Y.); wangmei@sxu.edu.cn (M.W.)

Abstract: Transition bimetallic alloy-based catalysts are regarded as attractive alternatives for the oxygen evolution reaction (OER), attributed to their competitive economics, high conductivity and intrinsic properties. Herein, we prepared $FeNi_3$/C nanorods with largely improved catalytic OER activity by combining hydrothermal reaction and thermal annealing treatment. The temperature effect on the crystal structure and chemical composition of the $FeNi_3$/C nanorods was revealed, and the enhanced catalytic performance of $FeNi_3$/C with an annealing temperature of 400 °C was confirmed by several electrochemical tests. The outstanding catalytic performance was assigned to the formation of bimetallic alloys/carbon composites. The $FeNi_3$/C nanorods showed an overpotential of 250 mV to afford a current density of 10 mA cm^{-2} and a Tafel slope of 84.9 mV dec^{-1}, which were both smaller than the other control samples and commercial IrO_2 catalysts. The fast kinetics and high catalytic stability were also verified by electrochemical impendence spectroscopy and chronoamperometry for 15 h. This study is favorable for the design and construction of bimetallic alloy-based materials as efficient catalysts for the OER.

Keywords: $FeNi_3$ alloy; nanorods; bimetallic; oxygen evolution reaction

Citation: Yu, X.; Pan, Z.; Zhao, Z.; Zhou, Y.; Pei, C.; Ma, Y.; Park, H.S.; Wang, M. Boosting the Oxygen Evolution Reaction by Controllably Constructing $FeNi_3$/C Nanorods. *Nanomaterials* **2022**, *12*, 2525. https://doi.org/10.3390/nano12152525

Academic Editors: Francesc Viñes Solana and Yuichi Negishi

Received: 12 June 2022
Accepted: 20 July 2022
Published: 22 July 2022

1. Introduction

There is a global consensus that producing hydrogen energy via electrochemical water splitting will lighten the burden of consuming energy from fossil fuels and replace unsustainable energy sources [1–5]. The oxygen evolution reaction (OER) is a half-reaction of the electrolysis of water, but the issue of slow reaction kinetics during the complicated four-electron transfer process critically needs to be solved [6,7]. The energy conversion efficiency of catalysts for practical water splitting is affected by the high overpotential and energy consumption of catalysts during the OER process [8,9]. Ruthenium dioxide (RuO_2) and iridium dioxide (IrO_2), as effective OER catalysts [10–12], can facilitate a combination of OH^- ions in the alkaline electrolyte for the OER. However, the high price and scarcity of resources restrict its wide application in energy conversion systems [13,14]. Therefore, cost-competitive catalysts with high catalytic activity urgently need to be explored.

Recently, earth-abundant and low-cost transition metal (TM)-based catalysts with improved catalytic OER stability have been an effective strategy for water splitting. Transition metal (i.e., Fe, Co, Ni, and Mo) oxides or hydroxides can form hydroxide intermediates during the OER process [15–18], but their high energy barrier and sluggish kinetics are still difficult to overcome due to fact of their poor conductivity [19–22]. Therefore, many

efforts have been reported on the study of TM-based derivatives with modification of the surface electronic structure [23,24] including metal phosphides [25,26], sulfides [27,28], and fluorides [29,30]. Bimetal-based catalysts have the merits of enhanced reactivity and abundant active sites by the adjusted electronic structure at the metal/metal interfaces, which are important for improving the electrocatalytic performance [31]. Meanwhile, bimetal-based catalysts can form more oxygen vacancies and reduce the adsorption energy of anions in electrolytes [32]. As demonstrated by many reports, the incorporation of Fe^{3+} into transition metal-based catalysts can significantly increase the reactivity and catalytic activity during the OER process [33,34]. The iron–nickel bimetallic catalyst near the top of a volcano plot shows an excellent catalytic OER performance [35–38]. Importantly, the introduction of a conductive matrix in a bimetal system is favorable for increasing the electronic conductivity and catalytic stability, such as graphene [39], nickel foam [40], and amorphous carbon [41]. A couple of FeNi alloys with carbon supports can significantly increase the electrical conductivity, and the controllable construction of an FeNi/C hybrid can provide fast ion diffusion and enhance the electrocatalytic stability during the OER process.

Herein, we report iron–nickel/carbon ($FeNi_3$/C) nanorods as an effective OER catalyst through hydrothermal and activation approaches. The nanorod morphology can increase the amount of exposed surface and the number of effective catalytic active sites, which are beneficial for increasing the electrochemical activity. The effect of the activation temperature on the crystallinity and catalytic OER behavior of the $FeNi_3$/C nanorods were studied by physical characterization and electrochemical tests. As the optimal temperature was 400 °C, the $FeNi_3$/C nanorods showed excellent OER performance. Only 250 mV of the overpotential was required at 10 mA cm^{-2} with a Tafel slope of 84.9 mV dec^{-1}. The improved electrochemical stability was studied by chronoamperometry, which was indexed to the effect of rough morphology and optimal composition.

2. Experimental Section

2.1. Synthesis of the $FeNi_3$/C Nanorods

A mixture of deionized (DI) water (12 mL) and ethylene glycol (36 mL), as the solvent to dissolve 200 mg of $NiCl_2 \cdot 6H_2O$ and 200 mg of $FeCl_2$, and 200 mg of oxalic acid were subsequently slowly added under continuous ultrasonication. The solution was transferred to a stainless-steel autoclave (100 mL) and maintained at 150 °C for 12 h. As the temperature naturally cooled down, the precipitate was repeatedly washed with DI water/ethanol and dried at 60 °C under vacuum conditions overnight to obtain the FeNi nanorods. The FeNi nanorods were further thermally activated at 400 °C for 2 h with flowing N_2 gas, and the target sample was named $FeNi_3$/C. The $FeNi_3$/C was thermally activated at 300 and 500 °C and labeled as $FeNi_3$/C-300 and $FeNi_3$/C-500. The related catalytic performances of $FeNi_3$/C-300 and $FeNi_3$/C-500 were compared. The synthetic process of the Fe nanorods and the Ni nanorods was the same as for the FeNi nanorods, and the precursor only included a single metal salt, either $FeCl_2$ or $NiCl_2 \cdot 6H_2O$. The samples were thermally activated at 400 °C, and the obtained powders were labeled as Fe/C and Ni/C nanorods for further use.

2.2. Characterization

The crystal structure was characterized by powder X-ray diffraction (XRD) (Bruker D8 Advance powder X-ray diffractometer, Cu Kα1, λ = 1.5405 Å, 40 KV, and 40 mA, Bruker, Saarbrucken, Germany). Scanning electron microscopy (SEM) images were obtained using an S-4800 II, Hitachi (Tokyo, Japan). The morphological structure was confirmed by transmission electron microscopy (TEM, Philips, TECNAI 12, Amsterdam, The Netherlands) and high-resolution transmission electron microscopy (HRTEM) (FEI Tecnai G2 F30 STWIN, 300 kV, FEI, Hillsboro, OR, USA). X-ray photoelectron spectroscopy was measured using a Thermo Science ESCALAB 250Xi (Thermofisher, Waltham, MA, USA).

2.3. Electrochemical Measurements

The electrochemical performance was performed using an electrochemical workstation (CHI 660E, Shanghai, China). The active material loaded on a glassy carbon electrode (GC, 3 mm diameter, 0.07 cm^{-2}), graphite rod, and saturated calomel electrode (SCE) acted as the working, counter, and reference electrodes, respectively. The potentials were calculated to the reversible hydrogen electrode (RHE) by E(RHE) = E(SCE) + 0.0591 × pH + 0.24 V. The catalyst ink was prepared by mixing 5 mg of catalyst, 950 µL of ethanol, and 50 µL of Nafion solution (5 wt.% Nafion^{TM} in lower aliphatic alcohols and water, 15–20% water) under bath sonication. Then, the catalyst ink (10 µL) was dropped onto the GC and naturally dried. All data are presented with IR compensation unless otherwise noted.

The polarization curves were measured as the potential from 1.04 to 1.64 V vs. RHE at 5 mV s^{-1}. Electrochemical impedance spectroscopy (EIS) was measured from 10^6 Hz to 10^{-2} Hz. One thousand CV cycles were measured within the potential ranging from 1.04 to 1.64 V vs. RHE in 1 M KOH at a scan rate of 150 mV s^{-1}, and a linear sweep was measured under a sweep rate of 5 mV s^{-1} after 1000 cycles. Chronoamperometry (CA) was tested at a voltage of 1.48 V for 15 h.

3. Results and Discussion

The iron–nickel alloy with conductive carbon ($FeNi_3$/C) nanorods were synthesized via facile hydrothermal and thermal treatment methods. The high reducibility of ethylene glycol as the solvent could strongly couple the metal ions with oxalic acid, and the content of iron was accurately controlled to adjust the morphology of catalysts. After activation at a high temperature of 400 °C, the carbon ligands decomposed into carbon materials, which can improve the conductivity of the catalysts. Finally, the $FeNi_3$/C nanorods were obtained.

To probe the morphological structure of the $FeNi_3$/C nanorods, scanning electron microscopy (SEM) was carried out. The FeNi nanorods were uniform and had an average length of 1.5 µm, as shown in Figure 1a, which was different from the Ni nanorods, which had irregular lengths, and the Fe nanorods, which had longer lengths of approximately 2 µm (Figure S1a,b). As a comparison to the precursors, the morphology of the FeNi nanorods was adjusted by the electrostatic interaction of metal ions, which is favorable for exposing abundant surface area. After thermal activation, the surfaces of the $FeNi_3$/C nanorods became relatively rough due to the formation of the $FeNi_3$ alloy and the decomposition of the carbon ligands (Figure 1b), which can provide abundant active sites. This morphology was further confirmed by transmission electron microscopy (TEM) images, as shown in Figure 1c. The average thickness of the nanorods was approximately determined to be 90 nm (Figure S2). Two d-spacings of 0.176 and 0.203 nm of the $FeNi_3$/C nanorods corresponded to the (200) and (111) planes of the $FeNi_3$ (Figure 1d). Figure 1e shows the corresponding selected area electron diffraction (SAED). The existence of concerned elements were found using energy-dispersive spectroscopy (EDS) (Figure S3a and Table S1), and the elemental mapping results confirmed that the distribution of the Fe, Ni, C, and O elements in $FeNi_3$/C was uniform (Figure 1f).

The change in the crystal structure of $FeNi_3$/C was characterized by X-ray diffraction (XRD) (Figure 2a). The broadened peak at 25.8° corresponded to the (002) plane of graphitic carbon. The characteristic peaks for the FeNi nanorods were indexed to the existence of $NiFe_2O_4$ (JCPDS card No. 54-0964). In comparison, the $FeNi_3$/C nanorods showed strong characteristic peaks at 44.2°, 52.0°, and 75.7º, owing to the (111), (200), and (220) planes of the $FeNi_3$ alloy (JCPDS card No. 38-0419), which is agreement with the TEM results. The disappearance of the diffraction peaks of $NiFe_2O_4$ for $FeNi_3$/C was attributed to the decomposition of metal oxides during thermal activation. Meanwhile, the effect of the annealing temperature on the crystallinity of the $FeNi_3$/C nanorods was studied by XRD analysis (Figure S3b), and the average crystal size of the $FeNi_3$/ nanorods was approximately 15.6 nm. As the activation temperature increased, the domain characteristic peaks of the $FeNi_3$/C nanorods became stronger than for $FeNi_3$/C-300, indicating the increased crystallinity due to the formation of $FeNi_3$ alloys. There were no obvious changes

in the characteristic peaks between $FeNi_3$/C and $FeNi_3$/C-500, demonstrating that the optimal temperature of 400 °C was high enough to form a stable catalyst.

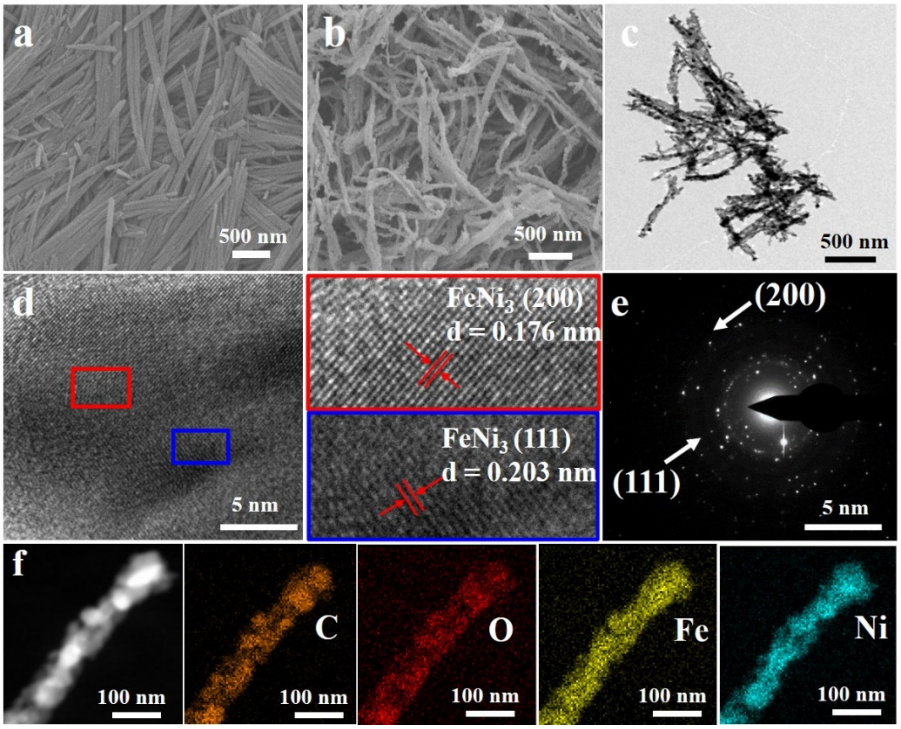

Figure 1. SEM images of (**a**) FeNi and (**b**) $FeNi_3$/C nanorods; (**c**) TEM and (**d**) HR-TEM images of $FeNi_3$/C nanorods; (**e**) SAED pattern; (**f**) STEM and elemental mappings of the $FeNi_3$/C nanorods.

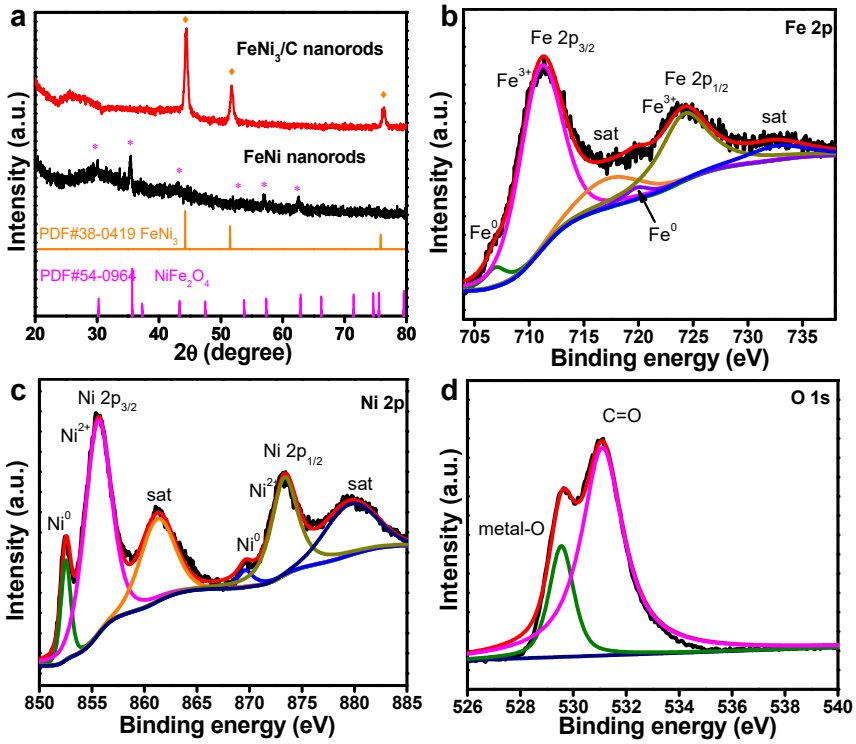

Figure 2. (**a**) XRD spectra of the FeNi and $FeNi_3$/C nanorods (the asterisk and oranges squares represent the diffraction peaks of $NiFe_2O_2$ and $FeNi_3$); high-resolution (**b**) Fe 2p, (**c**) Ni 2p, and (**d**) O1s XPS spectra of the $FeNi_3$/C nanorods.

The surface chemical circumstances of the $FeNi_3$/C nanorods were probed by X-ray photoelectron spectroscopy (XPS), and C 1s at 284.8 eV was applied to standardize the binding energy. From the full scan of the XPS spectra, the $FeNi_3$/C nanorods contained 11.6 atom% of O, 22.0 atom% of C, 19.5 atom% of Fe, and 46.9 atom% of Ni elements (Figure S4a). The C 1s spectra showed two dominant peaks at 284.8 eV for a C-C bond and at 288.6 eV for C-O bonds (Figure S4b). Figure 2b shows the deconvoluted Fe 2p spectra, and two distinct peaks were indexed to the spin-orbit coupling of Fe $2p_{1/2}$ and Fe $2p_{3/2}$ accompanying the satellite peaks. The peak was divided into Fe^0 (706.9 and 719.8 eV) and Fe^{3+} peaks (711.3 and 724.8 eV), respectively [42]. The Ni 2p spectra were deconvoluted into Ni^0 (852.5 and 869.7 eV) and Ni^{2+} (855.3 and 873.2 eV) with the related satellite peaks in Figure 2c [43], respectively. An energy difference of 17.8 eV was calculated between Ni $2p_{3/2}$ and Ni $2p_{1/2}$, implying that the Ni^{2+} state was dominant [44]. In addition, two peaks at 852.2 eV and 869.3 eV corresponded to Ni metal. The $FeNi_3$/C nanorods with contents of Fe^{3+} and Ni^{2+} can act as active material, and the electrocatalytic behavior can be dramatically affected by the boosted active sites arising from the conversion of Ni^{2+} to Ni^{3+} during the OER process [45]. The deconvoluted O 1s spectra are shown in Figure 2d, and the two peaks at 529.5 and 532.3 eV corresponded to metal-O and C=O bonds [41]. The existence of metal-O bonds can probably be ascribed to the formation of oxidized states on $FeNi_3$ alloy surfaces during thermal activation, and the internal high-oxygen coordination defects of the nanorods are generally considered as the dominant catalytic sites for increasing the oxidation kinetics and catalytic activity during the OER.

The electrocatalytic OER performance of the $FeNi_3$/C nanorods was initially evaluated by cyclic voltammetry (CV) using a three-electrode configuration, and an aqueous 1 M KOH was the electrolyte with N_2 purification. To reflect the effect of the activation temperature on the catalytic OER performance, the polarization curves of the $FeNi_3$/C nanorods were compared (Figure S5a). To receive a current density of 10 mA cm^{-2}, the overpotential of the $FeNi_3$/C nanorods (250 mV) was smaller than 280 mV for $FeNi_3$/C-300 and 290 mV for $FeNi_3$/C-500, and the Tafel slope for the $FeNi_3$/C nanorods (84.9 mV dec^{-1}) was lower than 99.2 and 101.1 mV dec^{-1} for $FeNi_3$/C-300 and $FeNi_3$/C-500 (Figure S5b). As shown in Figure 3a, the $FeNi_3$/C nanorods showed a lower overpotential at 10 mA cm^{-2} than that of Fe/C (370 mV), Ni/C (330 mV), commercial IrO_2/C (327 mV), and other reported FeNi-based electrocatalysts for the OER (Table S2). The low overpotential of $FeNi_3$/C implies a high OER activity due to the incorporation of Fe ions with Ni ions [46,47]. In addition, The Tafel slope can reflect the rate-determining step with the related reaction mechanism during the OER process, and Tafel slopes of 120, 60, and 40 mV represent the RSD of one-electron, chemical, and electron–proton reaction steps [48–50]. According to the Tafel slopes shown in Figure 3b, $FeNi_3$/C had a smaller value of 84.9 mV dec^{-1} compared to 102.2 and 121.2 mV dec^{-1} for Fe/C and Ni/C, indicating faster catalytic kinetics for $FeNi_3$/C. Chemical reactions with O_2 formation as an intermediate on the catalytic sites was dominant for $FeNi_3$/C, and the impact of the electron transfer process was no longer the primary step for the OER. The electrochemical dynamics and interfacial properties of the electrode were elucidated by electrochemical impedance spectroscopy (Figure 3c), and the calculated resistances are listed in Table S3 and were fit using Nyquist plots with an equivalent circuit in Figure S6. The charge transfer resistances (Rct) were 15.2, 110, and 26 Ω for the $FeNi_3$/C, Fe/C, and Ni/C nanorods, respectively. The smaller Rct value indicates a faster charge transfer behavior as well as higher catalytic activity of $FeNi_3$/C.

A catalyst exposing abundant active sites can show high electrochemical activity. The electrochemical surface area (ECSA) was estimated by CV measurement in a non-Faradic field (Table S4), and the double-layer capacitance (C_{dl}) value was calculated by linearly fitting the current density versus scan rates (Figure S7). Specific activity was obtained by normalizing the origin current to the ECSA. The $FeNi_3$/C nanorods with the optimal temperature of 400 °C had a specific activity of 0.24 mA cm^{-2} at the overpotential of 300 mV, which was higher than that of all control samples (Figure S8). The $FeNi_3$/C nanorods had a C_{dl} value of 4.14 mF cm^{-2}, as shown in Figure 3d, which was approximately 9.6 and

3.23 times higher than 0.43 and 1.28 mF cm^{-2} for Fe/C and Ni/C, respectively. This result confirms that $FeNi_3$/C provided an enlarged catalytic active surface for facilitating ion diffusion and promoting the electrochemical reaction.

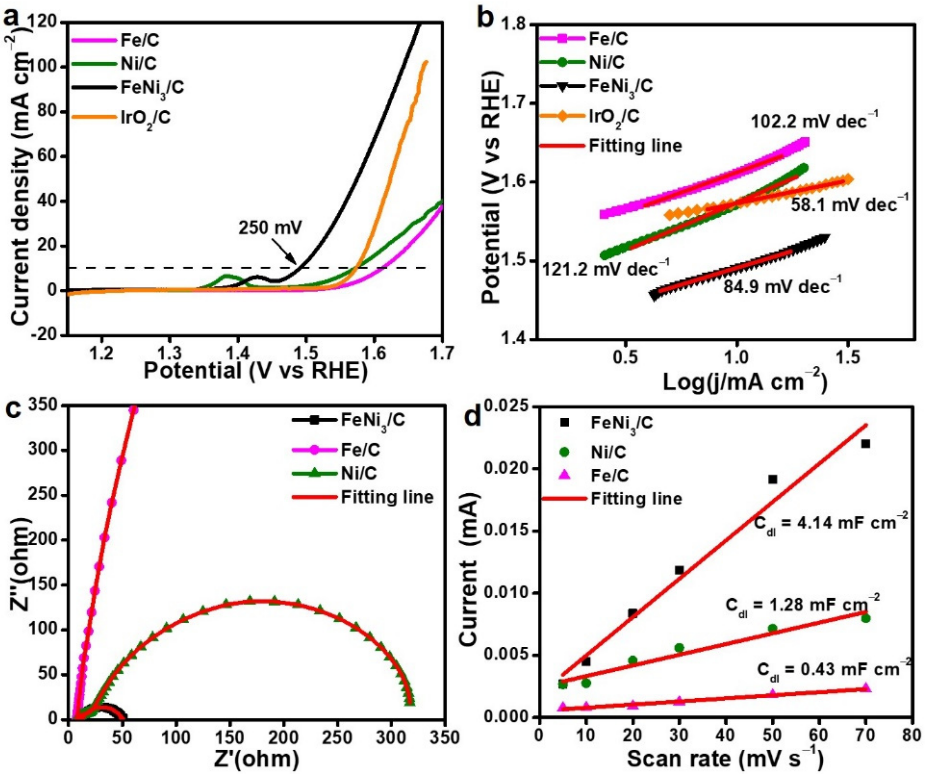

Figure 3. (**a**) Polarization curves of $FeNi_3$/C, IrO_2/C, Fe/C, and Ni/C nanorods at 5 mV s^{-1}; (**b**) Tafel slopes of $FeNi_3$/C, Fe/C, Ni/C, and IrO_2/C; (**c**) Nyquist plots; (**d**) C_{dl} values of $FeNi_3$/C, Fe/C, and Ni/C nanorods.

The long-term stability of the $FeNi_3$/C nanorods was initially evaluated by performing 1000 CV cycles, as shown in Figure 4a. The initial and 1001st CV curves almost overlap, and the overpotential at 10 mA cm^{-2} was a negligible change. Furthermore, chronoamperometry (CA) was measured at the potential of 1.48 V for 15 h (Figure 4b). The $FeNi_3$/C nanorods exhibited no obvious change in current density at the initial 10 h, and the current density remained at 90% for the next 5 h. The Faraday efficiency of $FeNi_3$/C was measured by comparing the experimental and theoretic amounts of oxygen gas produced during constant voltage electrolysis for 60 min (Figure S9), and the experimental volume was close to the theoretical oxygen volume, indicating that the oxygen evolution efficiency was close to 100%. These results demonstrate the outstanding electrocatalytic OER activity and stability of the $FeNi_3$/C nanorods, attributed to the in situ formation of the $FeNi_3$/C composites.

The morphological change of the $FeNi_3$/C surface after the stability test was characterized by TEM, as shown in Figure 5a. The morphology of $FeNi_3$/C nanorods was maintained, and the slight collapse or fracture phenomena were caused by the partial oxidation of $FeNi_3$ during the catalytic reaction in an alkaline solution. The change in the surface chemistry after the electrocatalytic test was confirmed by XPS. In comparison to the pristine state, the intensity of the metal-O bond after the CA test slightly increased with a shift of 0.4 eV because of the formation of intermediates. For the Ni element, the change in the Ni 2p spectra can be seen in Figure 5c, and the Ni $2p_{3/2}$ peak downshifted with by a value of 0.1 eV, attributed to the formation of nickel hydroxides or hydroxyl oxides after long-term CA testing. The Fe element showed a similar result, suggesting the formation of electroactive intermediates during the stability test, as shown in Figure 5d.

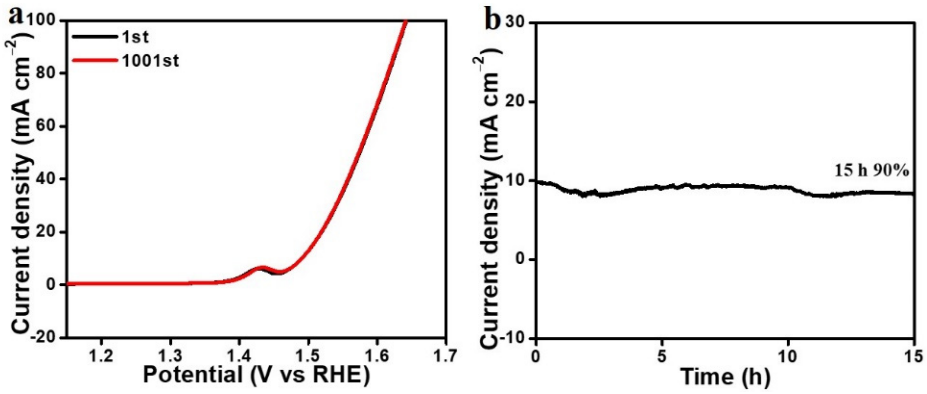

Figure 4. (**a**) The 1st and 1001st CV curves of $FeNi_3/C$; (**b**) chronoamperometry test of $FeNi_3/C$ at the potential of 1.48 V.

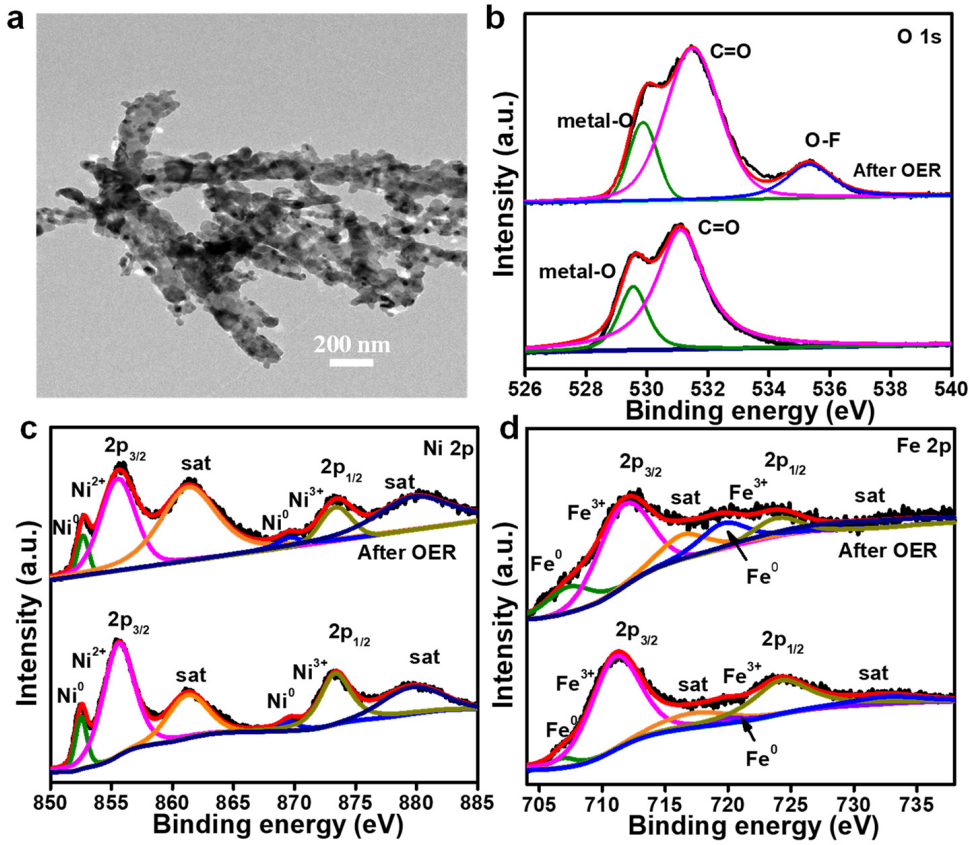

Figure 5. (**a**) TEM image of $FeNi_3/C$ after the stability test for the OER; (**b**–**d**) XPS spectrum of O 1s (**b**), Ni 2p (**c**), and Fe 2p (**d**) for the $FeNi_3/C$ alloy nanorod after the stability test for the OER.

During the OER process, the high-valence nickel in the catalysts was more conducive to the rapid formation of intermediates (Ni-OH) in the electrolyte, which was further combined with the OH^- to form a nickel oxyhydroxide followed by the removal of oxygen. Therefore, the high content of Ni^{2+} in $FeNi_3/C$ was more conducive to the OER, and the adjusted surface electronic structure by incorporation of Fe^{3+} increased the absorbability of OH^-, which resulted in the boosted catalytic activity of the catalysts during the OER process.

4. Conclusions

In summary, $FeNi_3$/C nanorods as effective catalysts for the OER were constructed by combining the facile hydrothermal reaction and further thermal annealing treatment. The temperature and compositional effect on the catalyst were discussed. The $FeNi_3$/C nanorods with an annealing temperature of 400 °C showed the best electrocatalytic performance such as a low overpotential of 250 mV at 10 mA cm^{-2}, small Tafel slope of 84.9 mV dec^{-1}, and high catalytic stability after CA testing for 15 h. The improved electrocatalytic behaviors were indexed to the controllable structure and optimal chemical composition by hybridizing bimetallic alloy with carbon. This work provides a strategy for preparing efficient catalysts for the OER by coupling bimetallic alloys with a carbon matrix.

Supplementary Materials: The following supporting information can be downloaded at: https://www.mdpi.com/article/10.3390/nano12152525/s1, Figure S1: SEM images of (a) Ni and (b) Fe nanorods; Figure S2: TEM image of $FeNi_3$/C nanorods; Figure S3; (a) EDS data of $FeNi_3$/C nanorods; (b) XRD patterns of $FeNi_3$/C nanorods with different thermal annealing temperatures; Figure S4: XPS spectrum of $FeNi_3$/C nanorods at (a) full scan and (b) C 1s; Figure S5: (a) Polarization curves and (b) Tafel plots of $FeNi_3$/C nanorods with different thermal annealing temperatures; Figure S6: The equivalent circuit model of the EIS analysis of all samples; Figure S7: CV curves of (a) $FeNi_3$/C nanorods; (b) Ni/C nanorods; (c) Fe/C nanorods at the potential of 1.04 V–1.14 V in 1 M KOH; Figure S8: (a) The specific activity of $FeNi_3$/C at different activation temperatures; (b) the specific activity of $FeNi_3$/C, Ni/C and Fe/C at the overpotential of 300 mV; Figure S9: Faraday efficiency of $FeNi_3$/C for OER; Table S1: The atomic ratio of all elements from EDS; Table S2: The comparison of other FeNi-based OER catalysts in alkaline medium; Table S3: EIS fitting parameters from equivalent circuits for as-prepared catalysts; Table S4: The value of C_{dl} and ECSA for $FeNi_3$/C with different annealing temperature. References [51–60] are cited in the Supplementary Materials.

Author Contributions: Conceptualization, Z.P. and Z.Z.; Formal analysis, Y.Z. and C.P.; Funding acquisition, X.Y., Y.M. and M.W.; Investigation, Y.Z. and C.P.; Methodology, Z.P. and Z.Z.; Project administration, X.Y.; Resources, X.Y.; Writing—original draft, Z.P. and Z.Z.; Writing—review and editing, X.Y., Y.M., H.S.P. and M.W. All authors have read and agreed to the published version of the manuscript.

Funding: This research was funded by the Natural Science Foundation of the Jiangsu Higher Education Institutions of China (18KJB150034); "Six Talent Peaks Project" in Jiangsu Province (XCL-104); "High-End Talent Project" of Yangzhou University; the National Natural Science Foundation of China (51902190); the Key Research and Development Program of Shanxi Province for International Cooperation (201803D421082); the Scientific and Technological Innovation Programs of Higher Education Institutions in Shanxi (2019L0013 and 2019L0018); the Shanxi Scholarship Council of China (2021-004).

Institutional Review Board Statement: Not applicable.

Informed Consent Statement: Not applicable.

Data Availability Statement: The data presented in this study are available on request from the corresponding author.

Acknowledgments: The authors would like to thank the anonymous reviewers who helped to significantly improve the quality of the research article.

Conflicts of Interest: The authors declare no conflict of interest.

References

1. Anantharaj, S.; Ede, S.R.; Karthick, K.; Sam Sankar, S.; Sangeetha, K.; Karthik, P.E.; Kundu, S. Precision and correctness in the evaluation of electrocatalytic water splitting: Revisiting activity parameters with a critical assessment. *Energy Environ. Sci.* **2018**, *11*, 744–771. [CrossRef]
2. Jiang, W.J.; Tang, T.; Zhang, Y.; Hu, J.S. Synergistic Modulation of Non-Precious-Metal Electrocatalysts for Advanced Water Splitting. *Acc. Chem. Res.* **2020**, *53*, 1111–1123. [CrossRef]
3. Guo, Y.; Tang, J.; Qian, H.; Wang, Z.; Yamauchi, Y. One-Pot Synthesis of Zeolitic Imidazolate Framework 67-Derived Hollow Co_3S_4@MoS_2 Heterostructures as Efficient Bifunctional Catalysts. *Chem. Mater.* **2017**, *29*, 5566–5573. [CrossRef]

4. Zhu, H.; Zhang, J.; Yanzhang, R.; Du, M.; Wang, Q.; Gao, G.; Wu, J.; Wu, G.; Zhang, M.; Liu, B.; et al. When cubic cobalt sulfide meets layered molybdenum disulfide: A core-shell system toward synergetic electrocatalytic water splitting. *Adv. Mater.* **2015**, *27*, 4752–4759. [CrossRef] [PubMed]
5. Kwon, I.S.; Debela, T.T.; Kwak, I.H.; Park, Y.C.; Seo, J.; Shim, J.Y.; Yoo, S.J.; Kim, J.G.; Park, J.; Kang, H.S. Ruthenium Nanoparticles on Cobalt-Doped 1T′ Phase MoS_2 Nanosheets for Overall Water Splitting. *Small* **2020**, *16*, 2000081. [CrossRef]
6. Zhuang, L.; Ge, L.; Yang, Y.; Li, M.; Jia, Y.; Yao, X.; Zhu, Z. Ultrathin iron-cobalt oxide nanosheets with abundant oxygen vacancies for the oxygen evolution reaction. *Adv. Mater.* **2017**, *29*, 1606793. [CrossRef]
7. Lu, B.; Cao, D.; Wang, P.; Wang, G.; Gao, Y. Oxygen evolution reaction on Ni-substituted Co_3O_4 nanowire array electrodes. *Int. J. Hydrogen Energy* **2011**, *36*, 72–78. [CrossRef]
8. Mom, R.V.; Cheng, J.; Koper, M.T.M.; Sprik, M. Modeling the oxygen evolution reaction on metal oxides: The infuence of unrestricted DFT calculations. *J. Phys. Chem. C* **2014**, *118*, 4095–4102. [CrossRef]
9. Zhang, J.; Zhao, Z.; Xia, Z.; Dai, L. A metal-free bifunctional electrocatalyst for oxygen reduction and oxygen evolution reactions. *Nat. Nanotechnol.* **2015**, *10*, 444–452. [CrossRef]
10. Li, C.; Baek, J.B. Recent Advances in Noble Metal (Pt, Ru, and Ir)-Based Electrocatalysts for Efficient Hydrogen Evolution Reaction. *ACS Omega* **2020**, *5*, 31–40. [CrossRef]
11. Reier, T.; Oezaslan, M.; Strasser, P. Electrocatalytic oxygen evolution reaction (OER) on Ru, Ir, and Pt catalysts: A comparative study of nanoparticles and bulk materials. *ACS Catal.* **2012**, *2*, 1765–1772. [CrossRef]
12. Park, S.; Shao, Y.; Liu, J.; Wang, Y. Oxygen electrocatalysts for water electrolyzers and reversible fuel cells: Status and perspective. *Energy Environ. Sci.* **2012**, *5*, 9331–9344. [CrossRef]
13. Stamenkovic, V.R.; Fowler, B.; Mun, B.S.; Wang, G.; Ross, P.N.; Lucas, C.A.; Marković, N.M. Improved oxygen reduction activity on $Pt_3Ni(111)$ via increased surface site availability. *Science* **2007**, *315*, 493–497. [CrossRef] [PubMed]
14. Zheng, Y.; Jiao, Y.; Zhu, Y.; Li, L.H.; Han, Y.; Chen, Y.; Jaroniec, M.; Qiao, S.-Z. High electrocatalytic hydrogen evolution activity of an anomalous ruthenium catalyst. *J. Am. Chem. Soc.* **2016**, *138*, 16174–16181. [CrossRef]
15. Wang, D.; Chen, X.; Evans, D.G.; Yang, W. Well-dispersed Co_3O_4/Co_2MnO_4 nanocomposites as a synergistic bifunctional catalyst for oxygen reduction and oxygen evolution reactions. *Nanoscale* **2013**, *5*, 5312–5315. [CrossRef]
16. Meng, Y.; Song, W.; Huang, H.; Ren, Z.; Chen, S.-Y.; Suib, S.L. Structure–property relationship of bifunctional MnO_2 nanostructures: Highly efficient, ultra-stable electrochemical water oxidation and oxygen reduction reaction catalysts identified in alkaline media. *J. Am. Chem. Soc.* **2014**, *136*, 11452–11464. [CrossRef]
17. Friebel, D.; Louie, M.W.; Bajdich, M.; Sanwald, K.E.; Cai, Y.; Wise, A.M.; Cheng, M.-J.; Sokaras, D.; Weng, T.-C.; Alonso-Mori, R.; et al. Identification of highly active Fe sites in (Ni,Fe)OOH for electrocatalytic water splitting. *J. Am. Chem. Soc.* **2015**, *137*, 1305–1313. [CrossRef]
18. Song, F.; Hu, X. Exfoliation of layered double hydroxides for enhanced oxygen evolution catalysis. *Nat. Commun.* **2014**, *5*, 4477. [CrossRef]
19. Yang, L.; Chen, L.; Yang, D.; Yu, X.; Xue, H.; Feng, L. NiMn layered double hydroxide nanosheets/$NiCo_2O_4$ nanowires with surface rich high valence state metal oxide as an efficient electrocatalyst for oxygen evolution reaction. *J. Power Sources* **2018**, *392*, 23–32. [CrossRef]
20. Chen, G.-F.; Ma, T.Y.; Liu, Z.-Q.; Li, N.; Su, Y.-Z.; Davey, K.; Qiao, S.-Z. Efficient and stable bifunctional electrocatalysts ni/nixmy (M = P, S) for overall water splitting. *Adv. Funct. Mater.* **2016**, *26*, 3314–3323. [CrossRef]
21. Xuan, C.; Wang, J.; Xia, W.; Peng, Z.; Wu, Z.; Lei, W.; Xia, K.; Xin, H.L.; Wang, D. Porous Structured Ni–Fe–P Nanocubes Derived from a Prussian Blue Analogue as an Electrocatalyst for Efficient Overall Water Splitting. *ACS Appl. Mater. Interfaces* **2017**, *9*, 26134–26142. [CrossRef] [PubMed]
22. Huang, C.; Zou, Y.; Ye, Y.-Q.; Ouyang, T.; Xiao, K.; Liu, Z.-Q. Unveiling the active sites of Ni–Fe phosphide/metaphosphate for efficient oxygen evolution under alkaline conditions. *Chem. Commun.* **2019**, *55*, 7687–7690. [CrossRef] [PubMed]
23. Zheng, S.; Guo, X.; Xue, H.; Pan, K.; Liu, C.; Pang, H. Facile one-pot generation of metal oxide/hydroxide@metal–organic framework composites: Highly efficient bifunctional electrocatalysts for overall water splitting. *Chem. Commun.* **2019**, *55*, 10904–10907. [CrossRef] [PubMed]
24. Li, Q.Y.; Zhang, L.; Xu, Y.X.; Li, Q.; Xue, H.; Pang, H. Smart Yolk/Shell ZIF-67@POM Hybrids as Efficient Electrocatalysts for the Oxygen Evolution Reaction. *ACS Sustain. Chem. Eng.* **2019**, *7*, 5027–5033. [CrossRef]
25. Li, D.; Liu, C.; Ma, W.; Xu, S.; Lu, Y.; Wei, W.; Zhu, J.; Jiang, D. Fe-doped NiCoP/Prussian blue analog hollow nanocubes as an efficient electrocatalyst for oxygen evolution reaction. *Electrochim. Acta* **2021**, *367*, 137492. [CrossRef]
26. Wang, F.; Yang, X.; Dong, B.; Yu, X.; Xue, H.; Feng, L. A FeP powder electrocatalyst for the hydrogen evolution reaction. *Electrochem. Commun.* **2018**, *92*, 33–38. [CrossRef]
27. Gao, M.-R.; Cao, X.; Gao, Q.; Xu, Y.-F.; Zheng, Y.-R.; Jiang, J.; Yu, S.-H. Nitrogen-doped graphene supported $CoSe_2$ nanobelt composite catalyst for efficient water oxidation. *ACS Nano* **2014**, *8*, 3970–3978. [CrossRef]
28. Dou, S.; Tao, L.; Huo, J.; Wang, S.; Dai, L. Etched and doped Co_9S_8/graphene hybrid for oxygen electrocatalysis. *Energy Environ. Sci.* **2016**, *9*, 1320–1326. [CrossRef]
29. Liu, H.; Zha, M.; Liu, Z.; Tian, J.; Hu, G.; Feng, L. Synergistically boosting the oxygen evolution reaction of an Fe-MOF via Ni doping and fluorination. *Chem. Commun.* **2020**, *56*, 7889–7892. [CrossRef]

30. Zha, M.; Pei, C.; Wang, Q.; Hu, G.; Feng, L. Electrochemical oxygen evolution reaction efficiently boosted by selective fluoridation of $FeNi_3$ alloy/oxide hybrid. *J. Energy Chem.* **2020**, *47*, 166–171. [CrossRef]
31. Jung, S.; McCrory, C.C.L.; Ferrer, I.M.; Peters, J.C.; Jaramillo, T.F. Benchmarking nanoparticulate metal oxide electrocatalysts for the alkaline water oxidation reaction. *J. Mater. Chem. A* **2016**, *4*, 3068–3076. [CrossRef]
32. Lyons, M.E.G.; Brandon, M.P. A comparative study of the oxygen evolution reaction on oxidised nickel, cobalt and iron electrodes in base. *J. Electroanal. Chem.* **2010**, *641*, 119–130. [CrossRef]
33. Trotochaud, L.; Young, S.L.; Ranney, J.K.; Boettcher, S.W. Nickel–Iron Oxyhydroxide Oxygen-Evolution Electrocatalysts: The Role of Intentional and Incidental Iron Incorporation. *J. Am. Chem. Soc.* **2014**, *136*, 6744–6753. [CrossRef]
34. Trześniewski, B.J.; Diaz-Morales, O.; Vermaas, D.A.; Longo, A.; Bras, W.; Koper, M.T.M.; Smith, W.A. In situ observation of active oxygen species in Fe-containing Ni-based oxygen evolution catalysts: The effect of pH on electrochemical activity. *J. Am. Chem. Soc.* **2015**, *137*, 15112–15121. [CrossRef] [PubMed]
35. Swierk, J.R.; Klaus, S.; Trotochaud, L.; Bell, A.T.; Tilley, T.D. Electrochemical study of the energetics of the oxygen evolution reaction at nickel iron (Oxy)hydroxide catalysts. *J. Phys. Chem. C* **2015**, *119*, 19022–19029. [CrossRef]
36. Jiang, J.; Zhang, C.; Ai, L. Hierarchical iron nickel oxide architectures derived from metal-organic frameworks as efficient electrocatalysts for oxygen evolution reaction. *Electrochim. Acta* **2016**, *208*, 17–24. [CrossRef]
37. Rossmeisl, J.; Qu, Z.W.; Zhu, H.; Kroes, G.J.; Nørskov, J.K. Electrolysis of water on oxide surfaces. *J. Electroanal. Chem.* **2007**, *607*, 83–89. [CrossRef]
38. Li, Q.; Song, Y.; Xu, R.; Zhang, L.; Gao, J.; Xia, Z.; Tian, Z.; Wei, N.; Rümmeli, M.H.; Zou, X.; et al. Biotemplating Growth of Nepenthes-like N-Doped Graphene as a Bifunctional Polysulfide Scavenger for Li–S Batteries. *ACS Nano* **2018**, *12*, 10240–10250. [CrossRef]
39. Wang, C.; Li, X.; Li, Q.; Pang, H. Graphene/Co_3O_4 composites in application of electrochemical energy conversion and storage. *FlatChem* **2019**, *16*, 100107. [CrossRef]
40. Muthurasu, A.; Maruthapandian, V.; Kim, H.Y. Metal-organic framework derived Co_3O_4/MoS_2 heterostructure for efficient bifunctional electrocatalysts for oxygen evolution reaction and hydrogen evolution reaction. *Appl. Catal. B Environ.* **2019**, *248*, 202–210. [CrossRef]
41. Liu, Z.; Yu, X.; Yu, H.; Xue, H.; Feng, L. Nanostructured FeNi3 Incorporated with Carbon Doped with Multiple Nonmetal Elements for the Oxygen Evolution Reaction. *ChemSusChem* **2018**, *11*, 2703–2709. [CrossRef] [PubMed]
42. Liu, L.; Yan, F.; Li, K.; Zhu, C.; Xie, Y.; Zhang, X.; Chen, Y. Ultrasmall $FeNi_3N$ particles with an exposed active (110) surface anchored on nitrogen-doped graphene for multifunctional electrocatalysts. *J. Mater. Chem. A* **2019**, *7*, 1083–1091. [CrossRef]
43. Yu, X.; Zhao, Z.; Pei, C. Surface oxidized iron-nickel nanorods anchoring on graphene architectures for oxygen evolution reaction. *Chin. Chem. Lett.* **2021**, *32*, 3579–3583. [CrossRef]
44. Zhang, B.; Xiao, C.; Xie, S.; Liang, J.; Chen, X.; Tang, Y. Iron–Nickel Nitride Nanostructures in Situ Grown on Surface-Redox-Etching Nickel Foam: Efficient and Ultrasustainable Electrocatalysts for Overall Water Splitting. *Chem. Mater.* **2016**, *28*, 6934–6941. [CrossRef]
45. Xue, Y.; Wang, Y.; Liu, H.; Yu, X.; Xue, H.; Feng, L. Electrochemical oxygen evolution reaction catalyzed by a novel nickel–cobalt-fluoride catalyst. *Chem. Commun.* **2018**, *54*, 6204–6207. [CrossRef]
46. Chung, D.Y.; Lopes, P.P.; Farinazzo Bergamo Dias Martins, P.; He, H.; Kawaguchi, T.; Zapol, P.; You, H.; Tripkovic, D.; Strmcnik, D.; Zhu, Y.; et al. Dynamic stability of active sites in hydr(oxy)oxides for the oxygen evolution reaction. *Nat. Energy* **2020**, *5*, 222–230. [CrossRef]
47. Dionigi, F.; Zeng, Z.; Sinev, I.; Merzdorf, T.; Deshpande, S.; Lopez, M.B.; Kunze, S.; Zegkinoglou, I.; Sarodnik, H.; Fan, D.; et al. In-situ structure and catalytic mechanism of NiFe and CoFe layered double hydroxides during oxygen evolution. *Nat. Commun.* **2020**, *11*, 2522. [CrossRef]
48. Suen, N.-T.; Hung, S.-F.; Quan, Q.; Zhang, N.; Xu, Y.-J.; Chen, H.M. Electrocatalysis for the oxygen evolution reaction: Recent development and future perspectives. *Chem. Soc. Rev.* **2017**, *46*, 337–365. [CrossRef] [PubMed]
49. Zhang, J.; Tao, H.B.; Kuang, M.; Yang, H.B.; Cai, W.; Yan, Q.; Mao, Q.; Liu, B. Advances in Thermodynamic-Kinetic Model for Analyzing the Oxygen Evolution Reaction. *ACS Catal.* **2020**, *10*, 8597–8610. [CrossRef]
50. Shinagawa, T.; Garcia-Esparza, A.T.; Takanabe, K. Insight on Tafel slopes from a microkinetic analysis of aqueous electrocatalysis for energy conversion. *Sci. Rep.* **2015**, *5*, 13801. [CrossRef]
51. Wang, J.; Li, K.; Zhong, H.-X.; Xu, D.; Wang, Z.-L.; Jiang, Z.; Wu, Z.-J.; Zhang, X.-B. Synergistic Effect between Met-al–Nitrogen–Carbon Sheets and NiO Nanoparticles for Enhanced Electrochemical Water—Oxidation Performance. *Angew. Chem. Int. Ed.* **2015**, *54*, 10530–10534. [CrossRef] [PubMed]
52. Narendra Kumar, A.V.; Li, Y.; Yu, H.; Yin, S.; Xue, H.; Xu, Y.; Li, X.; Wang, H.; Wang, L. 3D graphene aerogel sup-ported FeNi-P derived from electroactive nickel hexacyanoferrate as efficient oxygen evolution catalyst. *Electrochim. Acta* **2018**, *292*, 107–114. [CrossRef]
53. Li, Y.; Zhao, M.; Zhao, Y.; Song, L.; Zhang, Z. FeNi layered double-hydroxide nanosheets on a 3D carbon network as an efficient electrocatalyst for the oxygen evolution reaction. *Part. Part. Syst. Char.* **2016**, *33*, 158–166. [CrossRef]
54. Zhao, Y.; Chen, S.; Sun, B.; Su, D.; Huang, X.; Liu, H.; Yan, Y.; Sun, K.; Wang, G. Graphene-Co_3O_4 nanocomposite as electrocatalyst with high performance for oxygen evolution reaction. *Sci. Rep.* **2015**, *5*, 7629.

55. Yang, J.; Zhu, G.; Liu, Y.; Xia, J.; Ji, Z.; Shen, X.; Wu, S. Fe_3O_4-decorated Co9S8 nanoparticles in situ grown on re-duced graphene oxide: A new and efficient electrocatalyst for oxygen evolution reaction. *Adv. Funct. Mater.* **2016**, *6*, 4712–4721. [CrossRef]
56. Elizabeth, I.; Nair, A.K.; Singh, B.P.; Gopukumar, S. Multifunctional Ni-NiO-CNT composite as high performing free standing anode for Li ion batteries and advanced electro catalyst for oxygen evolution reaction. *Electrochim. Acta* **2017**, *230*, 98–105. [CrossRef]
57. Lu, X.; Zhao, C. Highly efficient and robust oxygen evolution catalysts achieved by anchoring nanocrystalline cobalt oxides onto mildly oxidized multiwalled carbon nanotubes. *J. Mater. Chem. A* **2013**, *1*, 12053–12059. [CrossRef]
58. Han, G.-Q.; Liu, Y.-R.; Hu, W.-H.; Dong, B.; Li, X.; Shang, X.; Chai, Y.-M.; Liu, Y.-Q.; Liu, C.-G. Three dimensional nickel oxides/nickel structure by in situ electro-oxidation of nickel foam as robust electrocatalyst for oxygen evolution reaction. *Appl. Surf. Sci.* **2015**, *359*, 172–176. [CrossRef]
59. Pei, C.; Chen, H.; Dong, B.; Yu, X.; Feng, L. Electrochemical oxygen evolution reaction efficiently catalyzed by a novel porous iron-cobalt-fluoride nanocube easily derived from 3-dimensional Prussian blue analogue. *J. Power Sources* **2019**, *424*, 131–137. [CrossRef]
60. Mao, S.; Wen, Z.; Huang, T.; Hou, Y.; Chen, J. High-performance bi-functional electrocatalysts of 3D crumpled graphene–cobalt oxide nanohybrids for oxygen reduction and evolution reactions. *Energ. Environ. Sci.* **2014**, *7*, 609–616. [CrossRef]